

1                   **Distribution of Earth's radiation belts protons over the drift**  
2                   **frequency of particles**

3                   **Alexander S. Kovtyukh**

4                   Skobeltsyn Institute of Nuclear Physics, Moscow State University, Moscow, 119234, Russia

5                   Correspondence: Alexander S. Kovtyukh (kovtyukhas@mail.ru)

6                   **Abstract.** On the data for the proton fluxes of the Earth's radiation belts (ERB) with energy  
7                   ranging from 0.2 to 100 MeV on the drift  $L$  shells ranging from 1 to 8, the quasi-stationary  
8                   distributions over the drift frequency  $f_d$  of protons around the Earth are constructed. For this  
9                   purpose, direct measurements of proton fluxes of the ERB in the period 1961–2017 near the  
10                  geomagnetic equator were employed. The main physical processes in the ERB manifested more  
11                 clearly in these distributions, and for protons with  $f_d > 0.5$  mHz at  $L > 3$  their distributions in the  
12                 space  $\{f_d, L\}$  have a more regular shape than in the space  $\{E, L\}$ . It has been found also that the  
13                 quantity of the ERB protons with  $f_d \sim 1\text{--}10$  mHz at  $L \sim 2$  does not decrease, as for protons with  
14                  $E > 10\text{--}20$  MeV (with  $f_d > 10$  mHz), but increases with an increase in solar activity. This means  
15                 that the balance of radial transport and losses of the ERB low-energy protons at  $L \sim 2$  is  
16                 disrupted in advantage of transport for these protons: the effect of an increase in the radial  
17                 diffusion rates with increasing solar activity, overpowers the effect of an increase in the density  
18                 of the dissipative medium.

19  
20  
21                  **Keywords.** Magnetospheric physics (energetic particles, trapped). Radiation belts.

22

## 23 **1 Introduction**

24 The Earth's radiation belts (ERB) consist mainly of charged particles with energy from  $E \sim 100$   
25 keV to several hundreds of megaelectronvolt (MeV). In the field of the geomagnetic trap, each  
26 particles of the ERB with energy  $E$  and equatorial pitch-angle  $\alpha_0$  ( $\alpha$  is the angle between the local  
27 vector of the magnetic field and the vector of a particle velocity) makes three periodic movements:  
28 Larmor rotation, oscillations along the magnetic field line, and drift around the Earth (Alfvén and  
29 Fälthammar, 1963; Northrop, 1963).

30 Three adiabatic invariants ( $\mu$ ,  $K$ ,  $\Phi$ ) correspond to these periodic motions of trapped particles,  
31 as well as three periods of time or three frequencies: a cyclotron frequency  $f_c$ , a frequency of  
32 particle oscillations along the magnetic field line  $f_b$ , and a drift frequency of particles around the  
33 Earth  $f_d$ . For the near-equatorial ERB protons, we have:  $f_c \sim 1\text{--}500$  Hz,  $f_b \sim 0.02\text{--}2$  Hz and  $f_d \sim 0.1\text{--}$   
34 20 mHz. The frequency  $f_c$  increases by tens to hundreds of times with the distance of the particle  
35 from the plane of the geomagnetic equator (in proportion to the local induction of the magnetic  
36 field), and the frequency  $f_b$  decreases by almost 2 times with increasing amplitude of particles  
37 oscillation.

38 The number of particles with a given frequency  $f_c$  decreases rapidly with an increase of  $L$ , and  
39 refers to higher and higher geomagnetic latitudes. For each given frequency  $f_b$ , particles become  
40 more and more energetic with an increase of  $L$  ( $E \propto L^2$ ) and their number becomes smaller.

41 Compared to the frequencies  $f_c$  and  $f_b$ , the drift frequency  $f_d$  for one particle species has a much  
42 narrower range of values; it does not depend on the mass of the particles and it very weakly  
43 depends on the amplitude of their oscillations (vary within  $\sim 20\%$ ); in this case, on each  $L$ -shell  
44 there are a significant number of particles corresponding to a certain value of  $f_d$ .

45 Therefore, it can be expected that the distributions of the ERB particles in the space  $\{f_d, L\}$  will  
46 have a more regular shape than in the space  $\{E, L\}$ , and the main physical processes in these belts  
47 will manifest themselves more clearly in these distributions. Furthermore, it can also be expected  
48 that on these more ordered background more fine features can be revealed that would not appear in  
49 the space  $\{E, L\}$ .

50 Despite the importance of the drift frequency  $f_d$  for the mechanisms of the ERB formation,  
51 reliable and sufficiently complete distributions of particles in the ERBs (over the frequency  $f_d$ )  
52 have not been presented nor analyzed; indeed, this is the first time.

53 The analysis presented in this paper is limited to the protons of the ERB during magnetically  
54 quiet periods of observations ( $Kp < 2$ ), when the proton fluxes and their spatial-energy  
55 distributions were quasi-stationary. In the following sections, the distributions of the ERB protons  
56 over their drift frequency  $f_d$  are constructed from experimental data (Sect. 2), and analyzed (Sect.  
57 3). The main conclusions of this work are given in Sect. 4.

## 58 **2 Constructing the distributions of the ERB protons over their drift frequency**

59 The problem of methodical differences in measurements of the fluxes of protons of the radiation  
60 belts on different satellites was one of the main ones in this work. From the published  
61 experimental data, one selected those that are in good agreement with each other and exclude from  
62 consideration all unreliable measurement results (with admixture of electrons and various ionic  
63 components of the ERB to the protons). Then, these reliable experimental results for proton fluxes  
64 and their anisotropy near the equatorial plane were represent in the space  $\{E, L\}$ ; this space is very  
65 efficient with respect to organizing experimental data obtained in different ranges of  $E$  and  $L$ .

66 In such representation of experimental data, there is no need for interpolation and extrapolation  
67 of fluxes on the energy (in other representations, such necessity arises due to differences in

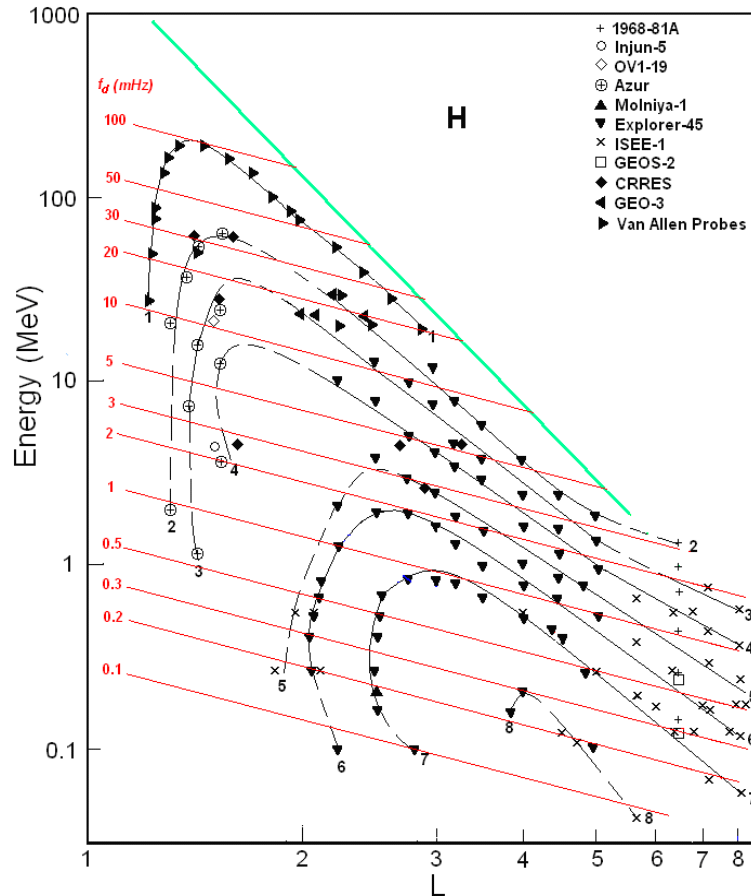
68 channel widths and their positions on the energy scale for instruments installed on different  
 69 satellites). In addition, with such a representation, in one figure, the data of various experiments, it  
 70 is possible to construct the isolines of fluxes (and anisotropy of fluxes); these isolines cannot  
 71 intersect with each other and, thus, allow to exclude a data that sharply fall out of the general  
 72 picture (for more details see in Kovtyukh, 2020).

## 73 2.1 Spatial-energy distributions of the ERB protons near the equatorial plane

74 To construct the distributions of the ERB particles over the drift frequency, it is necessary to have  
 75 reliable distributions of the differential fluxes of the ERB protons in the space  $\{E, L\}$ , where  $E$  is  
 76 the kinetic energy of protons and  $L$  is the drift shell parameter.

77 From the data of averaged satellite measurements of the differential fluxes of protons with an  
 78 equatorial pitch-angle  $\alpha_0 \approx 90^\circ$ , aforementioned distributions are constructed in (Kovtyukh, 2020)  
 79 during quiet periods ( $Kp < 2$ ) near solar activity maximum in 20th (1968–1971), 22th (1990–  
 80 1991), 23th (2000), and 24th (2012–2017) solar cycles. Such distributions, separately for minima  
 81 and maxima of the 11-year solar activity cycles, are constructed from satellite data also for other  
 82 ionic components of the ERB (near the equatorial plane), but the most reliable and detailed picture  
 83 was obtained in for protons (see Kovtyukh, 2020).

84 In Fig. 1 one of these distributions is reproduced for periods near solar maxima (on the data  
 85 from 1968 to 2017); here, data of different satellites are associated with different symbols. The  
 86 numbers on the curves (isolines) refers to the values of the decimal logarithms of the differential  
 87 fluxes  $J$  ( $\text{cm}^2 \text{ s sr MeV}^{-1}$ ) of protons (with equatorial pitch-angle  $\alpha_0 \approx 90^\circ$ ). The red lines  
 88 correspond to the dependences  $f_d(\text{mHz}) = 0.379 \cdot L \cdot E(\text{MeV})$  for the drift frequency of the near-  
 89 equatorial protons in the dipole approximation of the geomagnetic field.



91 **Figure 1.** Distribution of the differential fluxes  $J$  in the space  $\{E, L\}$  for protons with  $\alpha_0 \approx 90^\circ$  near maxima of the  
 92 solar activity (from Kovtyukh, 2020). Data of satellites are associated with different symbols. The numbers on the  
 93 curves refers to the values of the decimal logarithms of  $J$ . Fluxes is given in units of  $(\text{cm}^2 \text{ s sr MeV})^{-1}$ . The red lines  
 94 corresponds to the drift frequency  $f_d$ (mHz). The green line corresponds to the maximum energy of the trapped protons.

95 During quiet periods considered in this work, the geomagnetic field at  $L < 5$  is close to the  
 96 dipole configuration and  $L \approx L^*$  (see Roederer and Lejosne, 2018). At large  $L$ , the magnetic field  
 97 differs from the dipole one even in quiet periods; it is leads to the flattening of the isolines of the  
 98 proton fluxes at  $L > 5$  in Fig. 1.

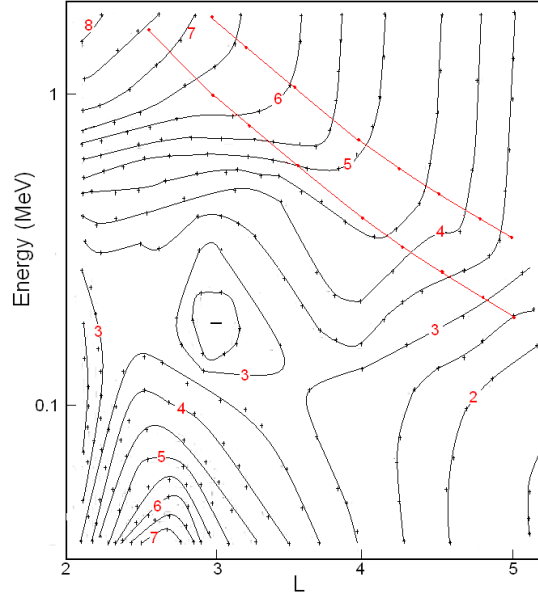
99 Only protons with energies less than some maximum values, determined by the Alfvén's  
 100 criterion:  $\rho_c(L, E) \ll \rho_B(L)$ , where  $\rho_c$  is the gyroradius of protons, and  $\rho_B$  is the radius of curvature  
 101 of the magnetic field (near the equatorial plane) can be trapped on the drift shells. According to  
 102 this criterion and to the theory of stochastic motion of particles, the geomagnetic trap in the dipolar  
 103 region can capture and durably hold only protons with  $E$  (MeV)  $< 2000 \cdot L^{-4}$  (Ilyin et al., 1984). The  
 104 green line in Fig. 1 represents this boundary.

105 The distribution of the ERB proton fluxes shown in Fig. 1, refers to the years of the solar  
 106 maximum, but the solar-cyclic variations in the ERB proton fluxes are small and localized at  $L <$   
 107 2.5 (see Kovtyukh, 2020).

## 108 **2.2 Spatial-energy distributions of the ERB protons outside the equatorial plane**

109 The quasi-stationary fluxes  $J$  of the ERB particles with given energy and local pitch-angle  $\alpha$   
 110 decrease usually when the point of observation is shifted from the equatorial plane to higher  
 111 latitudes along a certain magnetic field line. In the inner regions of the ERB, on  $L < 5$ , an angular  
 112 distributions of protons have usually a maximum at the local pitch-angle  $\alpha = 90^\circ$ . In wide interval  
 113 near this maximum these distributions are well described by the function  
 114  $J(\alpha, B/B_0) \propto (B/B_0)^{-A/2} \sin^A \alpha$  (Parker, 1957), where  $A$  is the index of an anisotropy of a  
 115 fluxes,  $B$  is the induction of a magnetic field at the point of measurements of these fluxes and  $B_0$  is  
 116 induction of a magnetic field at the equatorial plane on the same magnetic line.

117 The empirical model of an anisotropy  $A(E, L)$  for the proton fluxes with  $E \sim 0.1\text{--}2$  MeV on  $L \sim$   
 118 2–5 near the equatorial plane for the quasi-stationary ERB (for quiet periods with  $\text{Kp} < 2$ ) is  
 119 presented in Fig. 2. The anisotropy index  $A$  of these fluxes is shown in Fig. 2, in the space  $\{E, L\}$ ,  
 120 in the form of isolines with the same values  $A$  from 1.5 to 8.0 and with a step  $\Delta A = 0.5$ . The integer  
 121 values of this index are plotted on the corresponding isolines as red numbers.



122

123 **Figure 2.** Empirical model of the anisotropy index  $A(E, L)$  of the ERB proton fluxes averaged on the data of the  
 124 satellites obtained near the plane of the geomagnetic equator. Values of  $A$  are given on isolines of the anisotropy:  $A =$   
 125  $1.5\text{--}8.5$  with the step  $\Delta A = 0.5$ .

126 When constructing this model, we consider and analyze the data of the following satellites:  
 127 Explorer-12 (Hoffman and Bracken, 1965), Explorer-14 (Davis, 1965), Explorer-26 (Søraas and  
 128 Davis, 1968), OV1-14 and OV1-19 (Fennell et al., 1974), Explorer-45 (Williams and Lyons, 1974;  
 129 Fritz and Spjeldvik, 1981; Garcia and Spjeldvik, 1985), ISEE-1 (Garcia and Spjeldvik, 1985;  
 130 Williams and Frank, 1984), SCATHA (Blake and Fennell, 1981), Van Allen Probes (Shi et al.,  
 131 2016), and other satellites. These data were obtained in 1961-2015.

132 Fig. 2 shows that for rather high energy ( $> 1$  MeV) the anisotropy of a proton fluxes  
 133 monotonically increases with decreasing  $L$  (from  $A \sim 3.5$  to  $A \sim 8.0$ ). For  $E > 0.3$  MeV on  $L < 3$   
 134 anisotropy is monotonically increases with increasing energy, but for  $E > 0.5$  MeV on  $L > 3$  it is  
 135 almost energy-independent.

136 Some small irregularities of the isolines in Fig. 2 are due to the fact that experimental data were  
 137 used for constructing this figure were obtained in different years, with different instruments, and  
 138 during different intensity of the solar activity. At the same time, Fig. 2 demonstrates the important  
 139 regularities of the pitch-angle distributions of the quasi-stationary ERB proton fluxes.

140 In the region  $\{E > 0.5 \text{ MeV}, L > 3\}$  the isolines of the anisotropy index are almost parallel to  
 141 each other and to the energy axis. This adiabatic regularity refers to protons belonging to the  
 142 power-law tail of their energy spectra, the exponent of which practically does not change when  $L$   
 143 changes (at  $L > 3$ ). In Fig. 2, the red lines correspond to the lower boundary of the power-law tail  
 144 of the ERB protons energy spectra:  $E_b = (36 \pm 11) L^{-3} \text{ MeV}$  (see Kovtyukh, 2001, 2020).

145 The pattern of  $A(E, L)$  in the region on  $L > 3$  at  $E \sim 0.2\text{--}0.5$  MeV and the local minimum at  $L \sim$   
 146  $3$  ( $E \sim 0.2$  MeV) are connected with local maximum in the quasi-stationary proton energy spectra  
 147 of the ERB which corresponds to  $E = (17 \pm 3) L^{-3} \text{ MeV}$  (see Kovtyukh, 2001, 2020).

148 These regularities in the pattern of  $A(E, L)$  are explained within the framework of the theory of  
 149 radial transport (diffusion) of the ERB protons with conservation of the adiabatic invariants  $\mu$  and  
 150  $K$  of their periodic motions (these issues were most fully considered in Kovtyukh, 1993).

151 Both the local maximum at  $L \sim 2.5$  ( $E < 0.1$  MeV) and the region of low anisotropy at  $L \sim 2$  ( $E$   
 152  $\sim 0.1$  MeV) in Fig. 2, are related to the ionization losses of protons.

153 On the data of the satellites, the pitch-angle distributions of the ERB proton fluxes strongly  
 154 depend on MLT at  $L > 5$ : the average index  $A$  values on the day side are larger than on the night  
 155 side, and this dependence becomes more distinct with increasing energy (see, e.g., Shi et al., 2016).

156 These results indicate that drift shells splitting (Roederer, 1970) play an important role in the  
 157 formation of these distributions at  $L > 5$ . In the calculations performed here, it was assumed that  
 158 near the equatorial plane the pitch-angle distributions of the ERB proton fluxes at  $L > 6$ , averaged  
 159 over MLT, at  $\alpha_0 \sim 90^\circ$  are nearly isotropic.

160 High anisotropy for the fluxes of protons at  $E = 5\text{--}50$  MeV and a strong dependence  $A(L)$  at the  
 161 inner boundary of the inner belt ( $L = 1.15\text{--}1.40$ ,  $B/B_0 = 1.0\text{--}1.7$ ) were obtained on the satellite  
 162 DIAL (Fischer et al., 1977). According to these data, an anisotropy index increase from  $A \sim 12$  at  $L$   
 163  $= 1.25$  to  $A \sim 60$  at  $L = 1.15$ , and do not depends on  $L$  at  $L = 1.25\text{--}1.40$ . These results are supported  
 164 by the data of the satellite Resurs-01-N4 for the protons with  $E = 12\text{--}15$  MeV which were obtained  
 165 at  $h \sim 800$  km (Leonov et al., 2005). They will be taken into account in our calculations.

166 The experimental results on the pitch-angle distributions of the ERB proton fluxes and their  
 167 anisotropy indexes were discussed in detail in (Kovtyukh, 2018).

### 168 2.3 Drift frequency distributions of the ERB protons

169 Based on the results shown in Fig. 1 and 2, one can calculate the distributions of the ERB protons  
 170 over the drift frequency  $f_d$ . In these calculations, the dipole model of the geomagnetic field was  
 171 used, according to which (see, e.g., Roederer, 1970) the point of the magnetic field line at a given  
 172  $L$  and a geomagnetic latitude  $\lambda$  is located from the center of the dipole at a distance

$$173 \quad R(L, \lambda) = R_E L \cos^2 \lambda,$$

174 where  $R_E$  is the Earth's radius, and the field induction at a given  $L$  changes with changing  $\lambda$  as

$$175 \quad B(L, \lambda) = \frac{\sqrt{4 - 3 \cos^2 \lambda}}{\cos^6 \lambda} B_0(L),$$

176 where  $B_0(L) = 0.311 \text{ G} \times L^{-3}$ .

177 It was also taken into account that the drift frequency  $f_d$  of the nonrelativistic particles depends  
 178 essentially only on their kinetic energy  $E$  and on  $L$ . This value depends very slightly on the particle  
 179 pitch-angle: with an increase in the geomagnetic latitude of the mirror point of the particle trajectory  
 180 from  $0$  to  $10^\circ$ , it increases by only 1.5% and in the range from  $0$  to  $20\text{--}30^\circ$  it increases by 5.8–12.5%.

181 The number of protons with energies from  $E$  to  $E+dE$  per unit volume  $n$  is equal to the differential  
 182 flux of these particles  $J$  (falling per unit time per unit area of the detector per unit solid angle), divided  
 183 by the velocity  $v$  of these particles:  $n = J/v$ . For nonrelativistic protons with mass  $m$ , this velocity is  
 184  $(2E/m)^{1/2}$ .

185 Then in the near-equatorial region, between  $L$  and  $L+dL$  and within geomagnetic latitudes from  
 186  $0$  to  $\pm\lambda_0$ , the total number of nonrelativistic protons with mirror points within this region and with  
 187 energy from  $E$  to  $E+dE$ , drifting on a given  $L$  with frequency  $f_d(L, E)$  around the Earth, is

$$188 \quad \Delta N(L, f_d) = 2 \int_0^{\lambda_0} 2\pi R_E^2 L dL \frac{B_0(L)}{B(L, \lambda)} R_E L \cos \lambda \sqrt{4 - 3 \cos^2 \lambda} d\lambda \times$$

$$4\pi \int_{\alpha_{01}}^{\alpha_{02}} \frac{J(L, E(L, f_d)) dE}{\sqrt{2E(L, f_d)/m}} \sin^A \alpha_0 \cos \alpha_0 d\alpha_0,$$

189 where  $m$  is the rest mass of a proton,  $J(L, E(L, f_d))$  is the differential fluxes and  $E(L, f_d)$  is the  
 190 protons energy. The first integral takes into account that the magnetic flux in the layer between

191 shells  $L$  and  $L+dL$  it conserved when latitude  $\lambda$  changes, i.e.

$$192 \quad 2\pi R_E L \cos \lambda R_E dL = 2\pi R_E L \frac{B_0(L)}{B(L, \lambda)} R_E dL.$$

193 As result of integrating the last expression over  $\alpha_0$  and replacing  $\cos \lambda \equiv t$ , we obtain:

$$194 \quad \Delta N(L, f_d) = 4\pi R_E^3 L^2 dL \frac{J(L, E(L, f_d)) dE}{\sqrt{2E(L, f_d)/m}} \times \frac{4\pi}{A+1} \times$$

$$\int_{\cos \lambda_0}^1 t^7 \left[ \left( \frac{t^6}{\sqrt{4-3t^2}} \right)^{\frac{A+1}{2}} - (0.565)^{A+1} \right] dt$$

195 When integrating over equatorial pitch-angles  $\alpha_0$ , Liouville's theorem and the conservation of  
 196 the first adiabatic invariant ( $\mu$ ) are taken into account:  $\sin^2 \alpha_{01} = B_0(L)/B(L, \lambda_0)$  and  $\sin^2 \alpha_{02} =$   
 197  $B_0(L)/B(L, \lambda)$ , where  $B(L, 0) = B_0(L)$ .

198 With an increase  $\lambda$  from 0 to  $\lambda_0 = 30^\circ$ , the value of the function  $\sqrt{4-3t^2}$  increases from 1 to  
 199 1.32, i.e. deviates from the average value (1.16) by only 16%. Most part of the ERB protons are  
 200 concentrated at these latitudes. Therefore, when calculating the last integral, we will assume that  
 201  $\sqrt{4-3t^2} \approx 1.16$ .

202 Then you can get the following expression:

$$203 \quad \Delta N(L, f_d) = k \frac{J(L, E(L, f_d))}{\sqrt{E(L, f_d)}} F(A) L^2 dL dE,$$

204 where

$$205 \quad F(A) = \frac{1}{A+1} \left[ \frac{(1.16)^{-(A+1)/2}}{3A+11} (1 - 0.21 \cdot 0.65^A) - 0.085 (0.565)^{A+1} \right]$$

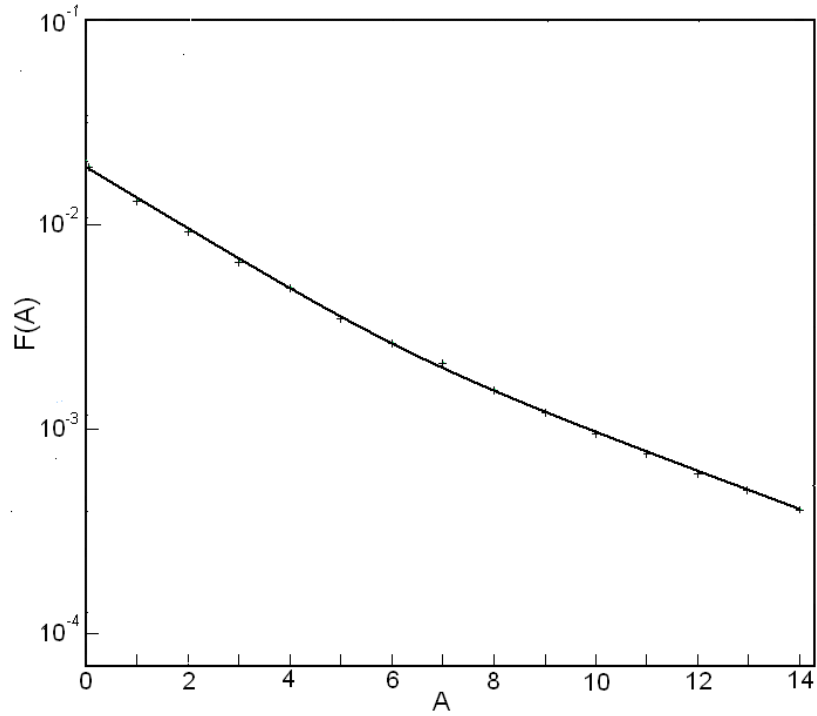
207 and

$$208 \quad k = (4\pi)^2 R_E^3 \sqrt{m/2} = 2.945 \cdot 10^{19} \text{ cm}^2 \text{ s sr MeV}^{1/2}.$$

209 When calculating the values of  $\Delta N$ , we will take that  $dL/L = dE/E = 0.1$ . Finally, for the  
 210 indicated ERB region near the equatorial plane, we obtain:

$$211 \quad \Delta N(L, f_d) = 2.945 \cdot 10^{17} J(L, E(L, f_d)) \sqrt{E(L, f_d)} F(A) L^3, \quad (1)$$

212 where  $J$ , the differential fluxes of protons with equatorially pitch-angle  $\alpha_0 \approx 90^\circ$ , is given in units  
 213 of  $(\text{cm}^2 \text{ s sr MeV})^{-1}$ , and the energy of protons  $E$  is given in MeV. The dependence  $F(A)$  is shown  
 214 in Fig. 3.

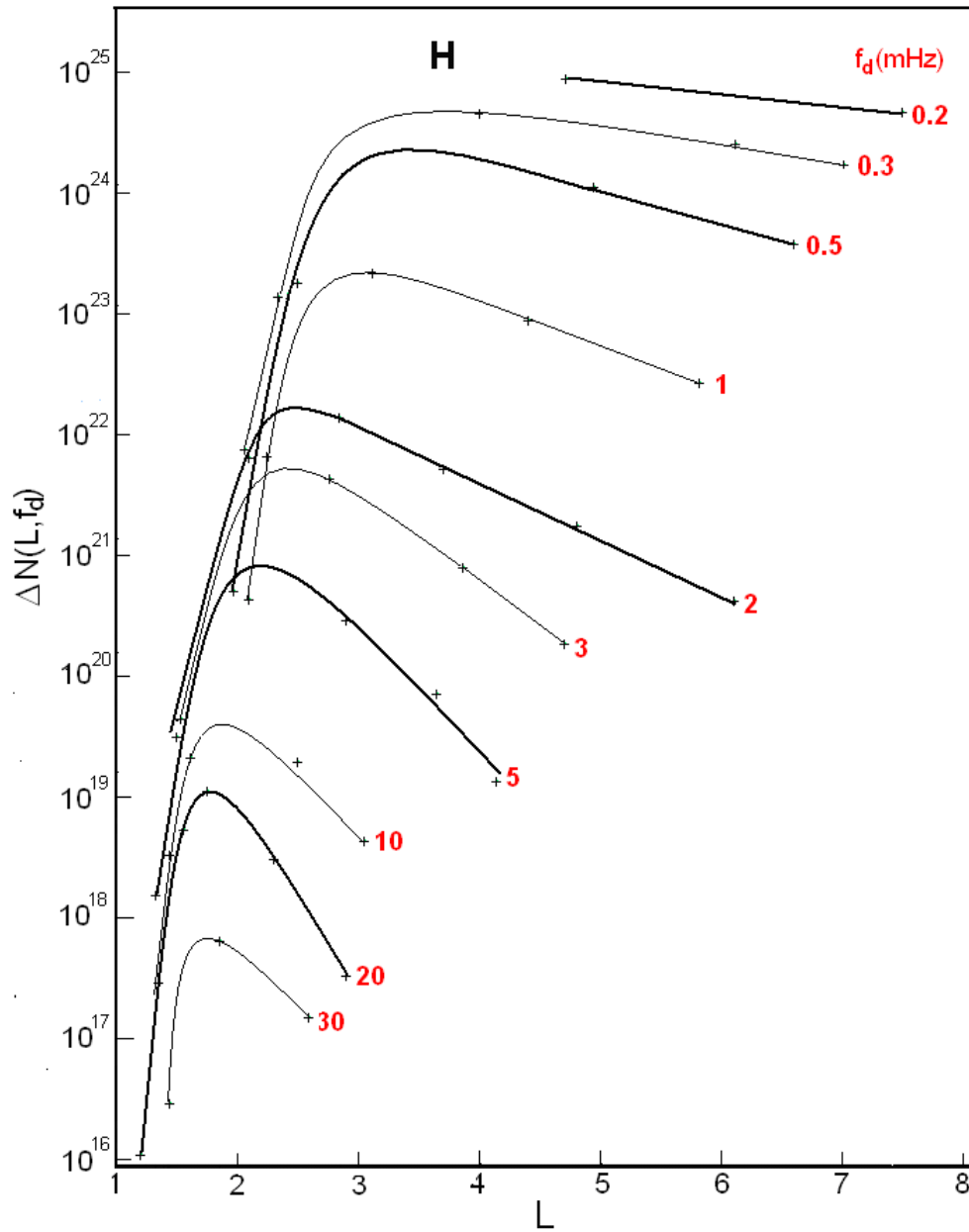


215

216 **Figure 3.** Dependence of the factor  $F(A)$  in formula (1) on the anisotropy index  $A$  of the proton fluxes.

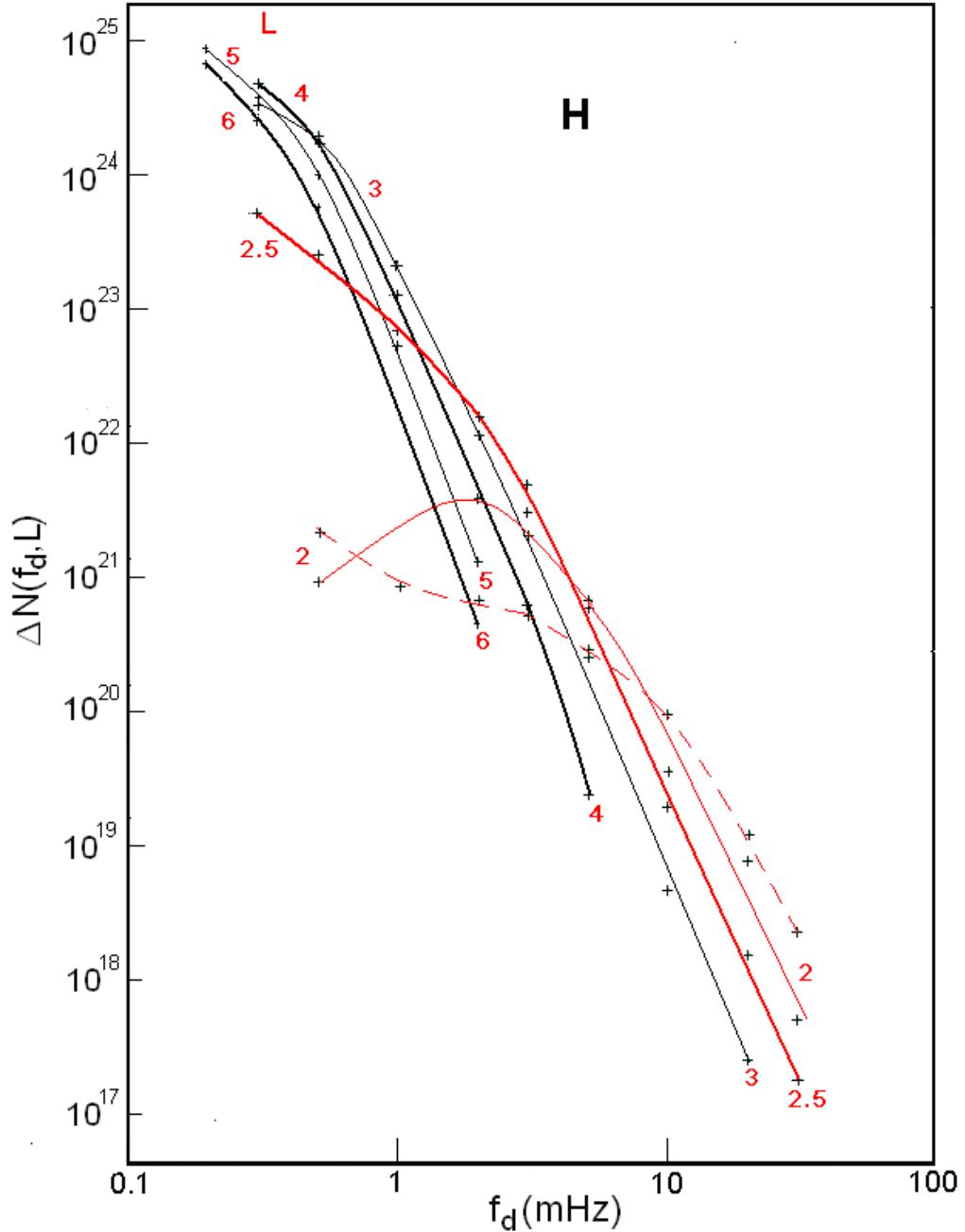
217 For protons of the ERB, the radial profiles  $\Delta N(L, f_d)$  for  $f_d = 0.2, 0.3, 0.5, 1, 2, 3, 5, 10, 20,$  and  
 218  $30$  mHz, calculated using the formula (1) together with Figs. 1–3 are shown in Fig. 4, and the  
 219 frequency spectra  $\Delta N(f_d, L)$  at  $L = 2, 2.5, 3, 4, 5,$  and  $6$  are shown in Fig. 5. Near each curve in Fig.  
 220 4, the corresponding value of  $f_d$ (mHz) is indicated, and each spectrum in Fig. 5 have the  
 221 corresponding  $L$  value (these values are highlighted in red). For clarity, in Figs. 4 and 5, thin  
 222 curves alternate with thick curves and in Fig. 5 spectra at  $L = 2$  and  $2.5$  are highlighted in red.





223

224 **Figure 4.** Radial profiles  $\Delta N(L, f_d)$  for protons of the ERB with drift frequencies  $f_d = 0.2, 0.3, 0.5, 1, 2, 3, 5, 10, 20$  and  
 225  $30$  mHz, plotted for periods of maximum solar activity. The  $f_d$  values corresponding to each curve are highlighted in  
 226 red. For clarity, thin curves are interspersed with thick curves.



227

228

229

230

231

**Figure 5.** Frequency spectra  $\Delta N(f_d, L)$  for protons of the ERB at  $L = 2, 2.5, 3, 4, 5$  and  $6$ , plotted for periods of maximum solar activity. The values  $L$  corresponding to each spectrum and spectra at  $L = 2$  and  $2.5$  are highlighted in red. The red dotted line shows the spectrum  $\Delta N(f_d, L)$  of the ERB protons at  $L = 2$ , constructed from data during minimum periods of solar activity (see Kovtyukh, 2020). For clarity, thin curves are interspersed with thick curves.

232

233

234

235

The errors of these calculations consist mainly of the errors of the averaged experimental data shown in Figs. 1 and 2 (these errors are most significant at  $L < 2$ ), and because of the deviations of the geomagnetic field from the dipole model at  $L > 5$ .

236

237

238

239

As  $\lambda_0$  decreases, the errors in our calculations will decrease. These errors can be reduced also by using numerical computer calculations. However, it should be taken into account that even in very quiet periods of observations the fluxes of the ERB protons, as well as the energy spectra and pitch-angle distributions of these fluxes, may experience changes that exceed the errors of our calculations.

240

### 3 Discussion

241 In agreement with the results of experimental and theoretical studies, at  $L > 2$ , the main mechanism  
242 for the formation of the ERB protons is the radial diffusion of particles from the outer boundary of  
243 the geomagnetic trap to the Earth under conservation the adiabatic invariants  $\mu$  and  $K$  (see, e.g.,  
244 Lejosne and Kollmann, 2020; Kovtyukh, 2016b, 2018).

245 Figs. 1 and 2 presented here make it possible to determine the regions of the  $\{E, L\}$  space near  
246 the equatorial plane in which the ionization losses of ions during their radial diffusion can be  
247 neglected and where they cannot.

248 The isolines of proton fluxes in Fig. 1 at sufficiently large  $E$  and  $L$  go up with decreasing  $L$ , in  
249 the direction of increasing energy, in strict agreement with the adiabatic laws of radial transport of  
250 particles. At lower  $L$  these isolines do change the direction of their course, under the influence of  
251 ionization losses, which increase rapidly with decreasing  $L$  (see in Kovtyukh, 2020 for details).

252 At sufficiently large values of  $E$  and  $L$ , isolines of the anisotropy index in Fig. 2 pass practically  
253 parallel to each other and parallel to the energy axis, in agreement with the laws of adiabatic  
254 transport of particles with power-law energy spectra (see Kovtyukh, 1993). At lower  $E$  and  $L$ , a  
255 more complex picture is formed under the influence of ionization losses (for more details see in  
256 Kovtyukh, 2001, 2018).

257 With decreasing  $L$ , the radial diffusion is decreased very rapidly, and the belt of protons with  $E$   
258  $> 10$ – $20$  MeV on  $L < 2$  is generated mainly as result of decay a neutrons of albedo which are  
259 knocked from the atmospheric atoms nuclei by the Galactic Cosmic Rays (GCR) protons. This  
260 mechanism (CRAND) is simulated in many contemporary studies based on the experimental data  
261 (see, e.g., Selesnick et al., 2007, 2013, 2014, 2018).

262 The mechanisms of formation of the ERB under the action of radial diffusion and CRAND are  
263 manifested and clearly differ both in the radial profiles  $\Delta N(L, f_d)$  and in the frequency spectra  
264  $\Delta N(f_d, L)$  of protons.

265 Let us consider the manifestations of these mechanisms in Fig. 4 and 5 and related effects.

266 In contrast to the radial profiles of fluxes  $J(L, E)$ , the radial profiles  $\Delta N(L, f_d)$  for protons with  $f_d$   
267  $< 5$  mHz (see Fig. 4) have much less steeper outer edges and their steepness decreases with  
268 decreasing frequency  $f_d$ . This effect is connected mainly with an increase in the volume of  
269 magnetic tubes (factor  $L^3$  in formula (1) from Section 2.3) and with a decrease in the anisotropy  
270 index of proton fluxes with increasing  $L$ .

271 At the same time, in comparison with the radial profiles  $J(L, E)$ , the radial profiles  $\Delta N(L, f_d)$   
272 have more steeper inner edges. This effect is mainly connected to the large anisotropy of proton  
273 fluxes in the corresponding region of space  $\{E, L\}$  and with the rapid growth of the anisotropy  
274 index with decreasing  $L$  in this region. It is especially expressed in the radial profiles  $\Delta N(L, f_d)$  at  $f_d$   
275  $\sim 0.3$ – $1$  mHz (see Fig. 4); this is due to the fact that in the corresponding region of space  $\{E, L\}$  the  
276 anisotropy index of proton fluxes strongly depends on  $E$  and  $L$  (see Fig. 2).

277 Radial profiles  $\Delta N(L, f_d)$  at  $f_d > 10$  mHz are formed by the mechanism CRAND. They have a  
278 maximum at  $L \sim 1.5$ – $2.0$ , and the steepness of their inner and outer edges does not differ as much  
279 as for lower frequencies  $f_d$  (see Fig. 4). When constructing these profiles, it was taken into account  
280 that at  $E = 5$ – $50$  MeV an anisotropy index  $A$  of proton fluxes do not depend on  $L$  at  $L = 1.25$ – $1.40$ :  
281  $A = 12 \pm 2$  (Fischer et al., 1977; Leonov et al., 2005).

282 The shape of the spectra  $\Delta N(f_d, L)$  at  $L > 3$  is determined, first of all, by the shape of the energy  
283 spectra of proton fluxes  $J(E, L)$  at the outer boundary of the geomagnetic trap. Gradually, as the  
284 particles diffuse to the Earth, their energy spectra are transformed under the action of betatron  
285 acceleration and ionization losses of particles.

286 In contrast to the energy spectra of proton fluxes  $J(E, L)$ , distributions  $\Delta N(f_d, L)$  of the ERB  
287 protons over their drift frequency  $f_d$  (Fig. 5) differ much less from each other at  $L > 3$ . Such  
288 convergence of the spectra  $\Delta N(f_d, L)$  is driven by increase in the volume of magnetic tubes and a

289 decrease in the anisotropy index of the ERB proton fluxes with increasing  $L$ . Fig. 5 demonstrates  
290 the closeness to the adiabatic transformations of the spectra  $\Delta N(f_d, L)$  when  $L$  changes at  $L > 3$ .

291 The energy spectra of near-equatorial proton fluxes  $J(E, L)$  with  $E > 10 \cdot L^{-3}$  MeV at  $L > 3$  in  
292 quiet periods have a local maximum at  $E = (17 \pm 3) \cdot L^{-3}$  MeV and a power-law tail ( $J \propto E^{-\gamma}$ , where  $\gamma$   
293  $= 4.25 \pm 0.75$ ) at  $E > (36 \pm 11) \cdot L^{-3}$  MeV (Kovtyukh, 2001, 2018, 2020).

294 The frequency spectra of the ERB protons at  $L > 3$  weakly depend on  $L$  and over the considered  
295 range  $\Delta f_d$  have a close to power-law shape with an exponent  $\gamma = 4.71 \pm 0.43$  (at  $f_d > f_d^*$ , where  $f_d^*$   
296  $\sim 0.5$  mHz at  $L \sim 3-6$ ,  $\sim 2$  mHz at  $L = 2.5$  and  $\sim 5$  mHz at  $L = 2$ ). Note that the spread of the  
297 parameter  $\gamma$  for the frequency spectra of protons is almost 2 times less than for their energy spectra.

298 These spectra become more rigid (flattened) at  $f_d < f_d^*$ .

299 Thus, the average exponents of the power-law tail of the energy and frequency spectra of  
300 protons differ by  $\Delta\gamma = 0.46$ , and there is no local maximum in the frequency spectra at  $f_d > 2$  mHz  
301 at  $L > 2.5$ . The main role in such differences in the shape of the energy and frequency spectra of  
302 protons was played by the factor  $F(A)$  in formula (1), in which the anisotropy index  $A$  is a function  
303 of  $E$  and  $L$  (see Figs. 2 and 3). Note that in the region  $\{E > 0.5 \text{ MeV}, L > 3\}$  the anisotropy index  
304  $A$ , as well as the protons energy, is transformed according to adiabatic laws when  $L$  changes (see  
305 Fig. 2 and comments to it).

306 These results confirm our hypothesis about the ordering of the distributions of protons over  
307 their drift frequency  $f_d$  in the outer regions of the ERB, at  $L > 3$ , where most of the ERB protons  
308 are located and where the radial diffusion of protons overpowers their ionization losses.

309 At all  $L$ , the frequency spectra  $\Delta N(f_d, L)$  become more flat at small  $f_d$  (at small  $E$ ) under  
310 influence ionization losses. However, in the range of high  $f_d$  (from 3–5 mHz to 30 mHz), for  
311 protons with high energies and low ionization losses, the protons frequency spectra have a power-  
312 law tail even at  $L = 2$  (see Fig. 5).

313 For protons with  $f_d < 0.5$  mHz, which correspond to the ERB protons of the lowest energies,  
314 ionization losses lead to the same consequences at higher  $L$ -shells: the radial profiles  $\Delta N(L, f_d)$   
315 approach each other, and the spectra  $\Delta N(f_d, L)$  flatten out (see Figs. 4 and 5).

316 In the region of the steep inner edge of the radial distributions  $\Delta N(L, f_d)$ , spectra  $\Delta N(f_d, L)$  of the  
317 ERB protons become gradually increasingly rigid with decreasing  $L$ , and rapidly diverge from each  
318 other (see Fig. 4 and 5). In the range of small  $f_d$  at  $L < 2.5$ , the connection between these  
319 distributions and the shape of the boundary energy spectra of protons is gradually lost.

320 These results indicate a violation of the order in the distributions of protons under the influence  
321 of ionization losses.

322 In Fig. 5, the dotted line also shows the spectrum  $\Delta N(f_d, L)$  of the ERB protons at  $L = 2$ ,  
323 constructed from experimental data for periods of low solar activity between the 19th/20th,  
324 20th/21th, 21th/22th, and 22th/23th solar cycles (see Fig. 1 in Kovtyukh, 2020). Fig. 5 show that at  
325  $L = 2$  for  $f_d > 10$  mHz there were more protons at the minimum of solar activity, and for  $f_d \sim 1-10$   
326 mHz there were more protons at the maximum of solar activity.

327 The effect of a decrease in the  $\Delta N(f_d, L)$  values for protons with  $f_d > 10$  mHz at  $L < 2$  with an  
328 increase in solar activity is mainly connected with a decrease in the fluxes of protons with  $E > 10-$   
329  $20$  MeV here. This effect is well known. It is described by the CRAND mechanism (see, e.g.,  
330 Selesnick et al., 2007) and was considered in detail in (Kovtyukh, 2020). With an increase in solar  
331 activity, the densities of atmospheric atoms and ionospheric plasma on small  $L$ -shells significantly  
332 increase, which leads to an increase in ionization losses of the ERB protons, and the power of their  
333 main source (CRAND) practically does not change. As a result, the equilibrium fluxes and  $\Delta N(f_d,$   
334  $L)$  for protons with  $f_d > 10$  mHz are established at lower levels.

335 However, the effect of an increase in  $\Delta N(f_d, L)$  for  $f_d \sim 1\text{--}10$  mHz at low  $L$  with increasing solar  
336 activity, corresponding to the protons of lower energies, was discovered here for the first time.

337 With decreasing  $E$  (and  $f_d$ ) of protons their ionization losses increase, and if the fluxes of low-  
338 energy protons in the inner belt were also formed by the CRAND mechanism, one would have  
339 observed even stronger increase of their fluxes with decreasing solar activity, than for protons with  
340  $E > 10\text{--}20$  MeV ( $f_d > 10$  mHz). But for protons with  $f_d \sim 1\text{--}10$  mHz, we see in Fig. 5 the opposite  
341 effect in the spectra  $\Delta N(f_d, L)$  at  $L = 2$ , which is not described by the CRAND mechanism.

342 On the other hand, it was proved that quasi-stationary fluxes of protons with  $E < 15$  MeV at  $L \sim$   
343  $2$  are formed mainly by the mechanism of protons radial diffusion from the external region of the  
344 ERB (Selesnick et al., 2007, 2013, 2014, 2018). These fluxes and  $\Delta N(f_d, L)$  values for  $f_d \sim 1\text{--}10$   
345 mHz at  $L = 2$  are formed as a result of a balance of competing processes radial diffusion of protons  
346 and their ionization losses.

347 The rates of transport of the ERB protons to the Earth (radial diffusion) rapidly increase with  
348 decreasing particles energy (see Kovtyukh, 2016b). In addition, with an increase in solar activity,  
349 the average level of geomagnetic fluctuations in the ERB increases. Under the influence of these  
350 factors, one can expect a significant increase in the intensity of radial diffusion of the low-energy  
351 protons at low  $L$  with an increase in solar activity. As a result, the effect of increasing in the  
352 density of a dissipative medium with an increase in solar activity is overpowered by a more  
353 significant effect of increasing in the rates of radial diffusion of protons.

354 According to numerous experimental data, during magnetic storms, a wide variety of complex  
355 spectra of powerful pulsations of magnetic and electric fields in the considered frequency range  
356 (ULF) can be generate in the geomagnetic trap, which are non-regularly distributed over  $L$ ; these  
357 pulsations can lead to local acceleration and losses of the ERB particles (see, e.g., Sauvaud et al.,  
358 2013). Such effects will violate the regular characteristics of the protons distributions shown in  
359 Fig. 4 and 5. However, during quiet periods ( $K_p < 2$ ), the amplitudes of such pulsations are small  
360 and they lead only to radial diffusion of particles.

## 361 **4 Conclusions**

362 From the data on near-equatorial ERB proton fluxes (with energy from 0.2 to 100 MeV and drift  $L$   
363 shells ranging from 1 to 8), their quasi-stationary distributions over the drift frequency of particles  
364 around the Earth ( $f_d$ ) were constructed. The results of calculations of the number  $\Delta N$  of the ERB  
365 protons within  $30^\circ$  in geomagnetic latitude at different  $L$  and  $f_d$  for periods of maximum solar  
366 activity are presented. They differ from the corresponding distributions of the ERB protons for  
367 periods of low solar activity only at  $L < 2.5$  (for comparison, the spectra of these distributions are  
368 given at  $L = 2$ ).

369 The radial profiles of these distributions  $\Delta N(L, f_d)$  have only one maximum that shifts toward  
370 the Earth with increasing  $f_d$ . In comparison to the proton fluxes profiles  $J(L, E)$ , the radial profiles  
371  $\Delta N(L, f_d)$  at  $f_d < 5$  mHz have steeper inner edges and flatter outer edges. However, the radial  
372 profiles  $\Delta N(L, f_d)$  at  $f_d > 10$  mHz, which are formed by the CRAND mechanism, have inner and  
373 outer edges with only slightly difference from each other for what concerns the steepness of their  
374 profiles.

375 In contrast to the energy spectra of proton fluxes  $J(E, L)$ , the frequency spectra  $\Delta N(f_d, L)$  of the  
376 ERB protons at  $L > 3$  are weakly dependent on  $L$  and, for sufficiently large  $f_d$  they have a nearly  
377 power-law shape with an exponent  $\gamma = 4.71 \pm 0.43$ . There is no local maximum in these spectra in  
378 the region  $\{f_d > 2 \text{ mHz}, L > 2.5\}$ , as in the corresponding  $J(E, L)$  spectra.

379 The main physical processes in the ERB (radial diffusion, ionization losses of particles and  
380 mechanism CRAND) manifested clearly in these distributions.

381 Distributions  $\Delta N(L, f_d)$  and  $\Delta N(f_d, L)$  of the ERB protons in the region  $\{f_d > 0.5 \text{ mHz}, L > 3\}$   
382 have a more regular shape than in the corresponding region of the space  $\{E, L\}$ . In these regions,  
383 there is the majority of the ERB protons, and their radial diffusion overpowers their ionization  
384 losses during the transport of particles to the Earth.

385 In the region of the steep inner edges of the radial distributions  $\Delta N(L, f_d)$ , the spectra  $\Delta N(f_d, L)$   
386 of protons rapidly diverge from each other with decreasing  $L$ , and at low frequencies these spectra  
387 become flatten. These results indicate a violation of the order in these distributions of protons  
388 under the influence of ionization losses.

389 With increasing solar activity, the number of protons  $\Delta N(f_d, L)$  at  $L \sim 2$  decreases for  $f_d > 10$   
390 mHz and increases for  $f_d \sim 1\text{--}10$  mHz. The effect at high  $f_d$ , corresponding to protons with  $E > 15$   
391 MeV, is well known and is described in the framework of the CRAND mechanism.

392 However, the opposite effect at low  $f_d$ , corresponding to the lower-energy protons, is discovered  
393 here for the first time. This effect can be associated with the fact that the low-frequency part of the  
394 spectrum  $\Delta N(f_d, L)$  of protons, even at  $L \sim 2$ , is mainly formed by the mechanism of protons  
395 transport from the outer regions of the ERB. This effect may indicate that with increasing solar  
396 activity, the average rates of radial diffusion of protons increase as well. For low-energy protons at  
397  $L \sim 2$ , the effect of increasing density of a dissipative medium with increasing solar activity is  
398 overpowered by the increase of the rates of radial diffusion of particles.

399 Comparing this result with the results for ions with  $Z \geq 2$  at  $L > 2.5$  (see Kovtyukh, 2020), one  
400 can conclude that the amplitude of solar-cyclic variations of the radial diffusion coefficient  $D_{LL}$   
401 increases with decreasing  $E$  and  $L$  ( $Z$  is the charge of the atomic nucleus with respect to the charge  
402 of the proton).

403

404 *Data availability.* All data from this investigation are presented in Figs. 1–5.

405 *Competing interests.* The author declares that there is no conflict of interest.

406 *Acknowledgements.* The author is very grateful to the reviewers for their important and fruitful  
407 comments and proposals regarding the paper and to topical editor, Dr. Elias Roussos, for editing  
408 this paper.

409 *Review statement.* This paper was edited by Elias Roussos and reviewed by two anonymous  
410 referees.

411

412

413 **References**

- 414 Alfvén, H., and Fälthammar, C.-G.: *Cosmical Electrodynamics, Fundamental Principles*,  
 415 Clarendon Press, Oxford, 1963.
- 416 Davis, L. R.: Low energy trapped protons and electrons, *Proc. Plasma Space Sci. Symp.*, Eds. D.  
 417 B. Chang and C. Y. Huang, Washington, P. 212–226, 1965.
- 418 Fennell, J. F., Blake, J. B., and Paulikas, G. A.: Geomagnetically trapped alpha particles, 3. Low-  
 419 altitude outer zone alpha-proton comparisons, *J. Geophys. Res.*, **79**(4), 521–528,  
 420 <https://doi.org/10.1029/JA079i004p00521>, 1974.
- 421 Fischer, H. M., Auschrat, V. W., and Wibberenz, G.: Angular distribution and energy spectra of  
 422 protons of energy  $5 \leq E \leq 50$  MeV in the lower edge of the radiation belt in equatorial latitudes,  
 423 *J. Geophys. Res.*, **82**(4), 537–547, <https://doi.org/10.1029/JA082i004p00537>, 1977.
- 424 Fritz, T. A., and Spjeldvik, W. N.: Steady-state observations of geomagnetically trapped energetic  
 425 heavy ions and their implications for theory, *Planet. Space Sci.*, **29**(11), 1169–1193,  
 426 [https://doi.org/10.1016/0032-0633\(81\)90123-9](https://doi.org/10.1016/0032-0633(81)90123-9), 1981.
- 427 Garcia, H. A., and Spjeldvik, W. N.: Anisotropy characteristics of geomagnetically trapped ions, *J.*  
 428 *Geophys. Res.*, **90**(A1), 359–369, <https://doi.org/10.1029/JA090iA01p00359>, 1985.
- 429 Hoffman, R. A., and Bracken, P. A.: Magnetic effects of the quiet-time proton belt, *J. Geophys.*  
 430 *Res.*, **70**(15), 3541–3556, <https://doi.org/10.1029/JZ070i015p03541>, 1965.
- 431 Ilyin, B. D., Kuznetsov, S. N., Panasyuk, M. I., and Sosnovets, E. N.: Non-adiabatic effects and  
 432 boundary of the trapped protons in the Earth's radiation belts, *Bulletin of the Russian Academy*  
 433 *of Sciences: Physics*, **48**(11), 2200–2203, 1984.
- 434 Kovtyukh, A. S.: Relation between the pitch-angle and energy distributions of ions in the Earth's  
 435 radiation belts, *Geomagn. Aeron.*, **33**(4), 453–460, 1993.
- 436 Kovtyukh, A. S.: Geocorona of hot plasma, *Cosmic Res.*, **39**(6), 527–558,  
 437 <https://doi.org/10.1023/A:1013074126604>, 2001.
- 438 Kovtyukh, A. S.: Radial dependence of ionization losses of protons of the Earth's radiation belts,  
 439 *Ann. Geophys.*, **34**(1), 17–28, <https://doi.org/10.5194/angeo-34-17-2016>, 2016a.
- 440 Kovtyukh, A. S.: Deduction of the rates of radial diffusion of protons from the structure of the  
 441 Earth's radiation belts, *Ann. Geophys.*, **34**(11), 1085–1098, [https://doi.org/10.5194/angeo-34-](https://doi.org/10.5194/angeo-34-1085-2016)  
 442 [1085-2016](https://doi.org/10.5194/angeo-34-1085-2016), 2016b.
- 443 Kovtyukh, A. S.: Ion Composition of the Earth's Radiation Belts in the Range from 100 keV to  
 444 100 MeV/nucleon: Fifty Years of Research, *Space Sci. Rev.*, **214**(8), 124:1–124:30,  
 445 <https://doi.org/10.1007/s11214-018-0560-z>, 2018.
- 446 Kovtyukh, A. S.: Earth's radiation belts' ions: patterns of the spatial-energy structure and its solar-  
 447 cyclic variations, *Ann. Geophys.*, **38**(1), 137–147, [doi:10.5194/angeo-38-137-2020](https://doi.org/10.5194/angeo-38-137-2020), 2020.
- 448 Lejosne, S., and Kollmann, P.: Radiation Belt Radial Diffusion at Earth and Beyond, *Space Sci.*  
 449 *Rev.*, **216**(1), 19:1–19:78, <https://doi.org/10.1007/s11214-020-0642-6>, 2020.
- 450 Leonov, A., Cyamukungu, M., Cabrera, J., Leleux, P., Lemaire, J., Gregorie, G., Benck, S.,  
 451 Mikhailov, V., Bakaldin, A., Galper, A., Koldashov, S., Voronov, S., Casolino, M., De Pascale,  
 452 M., Picozza, P., Sparvulli, R., Ricci, M.: Pitch-angle distribution of trapped energetic protons  
 453 and helium isotop nuclei measured along the Resurs-01 No.4 LEO satellite, *Ann. Geophys.*,  
 454 **23**(8), 2983–2987, <https://doi.org/10.5194/angeo-23-2983-2005>, 2005.
- 455 Northrop, T. G.: *The Adiabatic Motion of Charged Particles*, Wiley-Interscience, NY, USA, 1963.
- 456 Parker, E. N.: Newtonian development of the dynamical properties of ionized gases of low density,  
 457 *Phys. Rev.*, **107**(4), 924–933. <https://doi.org/10.1103/PhysRev.107.924>, 1957.
- 458 Roederer, J. G.: *Dynamics of Geomagnetically Trapped Radiation*, Springer, NY, USA,  
 459 <https://doi.org/10.1007/978-3-642-49300-3>, 1970.

- 460 Roederer, J. G., and Lejosne, S.: Coordinates for representing radiation belt particle flux, *J.*  
461 *Geophys. Res. Space Physics*, **123**(2), 1381–1387, <https://doi.org/10.1002/2017JA025053>,  
462 2018.
- 463 Sauvaud, J.-A., Walt, M., Delcourt, D., Benoist, C., Penou, E., Chen, Y., and Russell C. T.: Inner  
464 radiation belt particle acceleration and energy structuring by drift resonance with ULF waves  
465 during geomagnetic storms, *J. Geophys. Res. Space Physics*, **118**(4), 1723–1736,  
466 <https://doi.org/10.1002/jgra.50125>, 2013.
- 467 Selesnick, R. S., Looper, M. D., and Mewaldt, R. A.: A theoretical model of the inner proton  
468 radiation belt, *Space Weather*, **5**(4), S04003, <https://doi.org/10.1029/2006SW000275>, 2007.
- 469 Selesnick, R. S., Hudson, M. K., and Kress B. T.: Direct observation of the CRAND proton  
470 radiation belt source, *J. Geophys. Res. Space Phys.*, **118**(12), 7532–7537,  
471 <https://doi.org/10.1002/2013JA019338>, 2013.
- 472 Selesnick, R. S., Baker, D. N., Jaynes, A. N., Li, X., Kanekal, S. G., Hudson, M. K., and Kress, B.  
473 T.: Observations of the inner radiation belt: CRAND and trapped solar protons, *J. Geophys.*  
474 *Res. Space Phys.*, **119**(8), 6541–6552, <https://doi.org/10.1002/2014JA020188>, 2014.
- 475 Selesnick, R. S., Baker, D. N., Kanekal, S. G., Hoxie, V. C., and Li, X.: Modeling the proton  
476 radiation belt with Van Allen Probes Relativistic Electron-Proton Telescope data, *J. Geophys.*  
477 *Res. Space Phys.*, **123**(1), 685–697, <https://doi.org/10.1002/2017JA024661>, 2018.
- 478 Shi, R., Summers, D., Ni, B., Manweiler, J. W., Mitchell, D. G., and Lanzerotti, L. J.: A statistical  
479 study of proton pitch-angle distributions measured by the Radiation Belt Storm Probes Ion  
480 Composition Experiment, *J. Geophys. Res. Space Phys.*, **121**(6), 5233–5249,  
481 <https://doi.org/10.1002/2015JA022140>, 2016.
- 482 Shi, R., Summers, D., Ni, B., Manweiler, J. W., Mitchell, D. G., and Lanzerotti, L. J.: A statistical  
483 study of proton pitch-angle distributions measured by the Radiation Belt Storm Probes Ion  
484 Composition Experiment, *J. Geophys. Res. Space Phys.*, **121**(6), 5233–5249,  
485 <https://doi.org/10.1002/2015JA022140>, 2016.
- 486 Søråas, F., and Davis, L.R.: Temporal variations of 100 keV to 1700 keV trapped protons observed  
487 on satellite Explorer 26 during first half of 1965, Rep. X-612-68-328, NASA Goddard Space  
488 Flight Cent., Greenbelt, Md., 1968.
- 489 Williams, D. J., and Lyons, L. R.: The proton ring current and its interaction with plasmopause:  
490 Storm recovery phase, *J. Geophys. Res.*, **79**(28), 4195–4207,  
491 <https://doi.org/10.1029/JA079i028p04195>, 1974.
- 492 Williams, D. J., and Frank, L. A.: Intense low-energy ion populations at low equatorial altitude, *J.*  
493 *Geophys. Res.*, **89**(A6), 3903–3911, <https://doi.org/10.1029/JA089iA06p03903>, 1984.